UNIVERSITY OF CAMBRIDGE

Imperial College London

NERC SCIENCE OF THE ENVIRONMENT

Supplementary material for: "Deep Mantle Contributions to African Volcanism Revealed by Absolute P-wave Tomography and Transition-Zone Receiver Functions"

A. Boyce[1], S. Cottaar[1] , I. D. Bastow[2] , R. Kounoudis[2]

[1]University of Cambridge, Earth Sciences, Cambridge, United Kingdom.
[2]Imperial College London, London, United Kingdom.

T028-03

ab2568@cam.ac.uk

alistairboyce11.github.io

Outline

Methodological details to accompany Virtual AGU presentation (T028-03) by A. Boyce and coauthors.

The slides are optimized for viewing on a large screen.

Resources and **References** are included.

AFRP20: African continental P-wave tomographic model

From relative to absolute travel-times

- Temporary networks yield low SNR waveforms.
- Because first breaking energy is often hidden by the noise, these data are routinely processed for relative arrival-times (e.g., VanDecar and Crosson, 1990).
- Need to recover background mean velocity structure to measure absolute arrival-times compatible with global tomographic models.
- We process 6 small aperture sub-regions (a) for absolute arrival times using the Absolute Arrival-time Recovery Method (AARM: Boyce et al., 2017).
- AARM capitalizes on optimized phase-weighted stacking to obtain a common time correction for each earthquake (T_{corr}). See next slide.

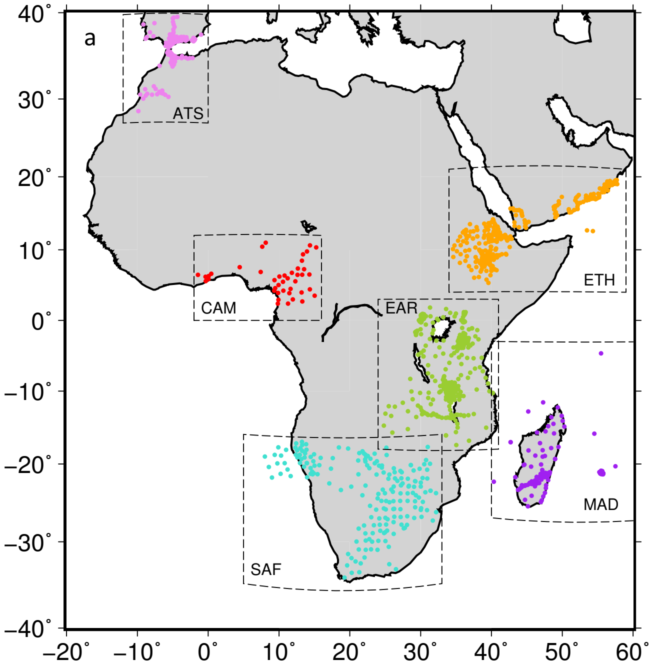

The Absolute Arrival-time Recovery Method: AARM

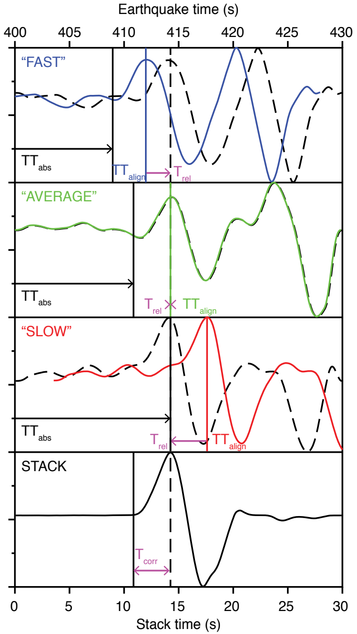

$TT_{abs} = TT_{align} + T_{corr}$

Trace	TT_{align}	T_{corr}	TT_{abs}
"Fast"	412	-3	409
"Average"	414	-3	411
"Slow"	417	-3	414

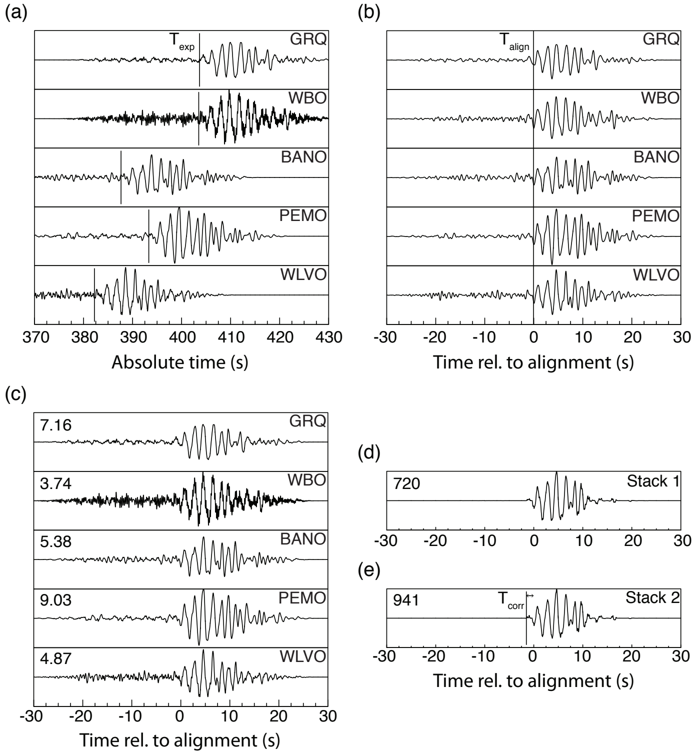

Transfer alignments into unfiltered data

↓

Stack waveforms for the earthquake

↓

Calculate weights to improve stack

↓

Restack weighted waveforms

↓

Pick first break on stack

↓

Calculate T_{corr}

↓

Compute absolute arrival times

Pick errors 0.15-0.2s

Boyce et. al., (2017)

Global P-wave tomography

- >21m rays – `EHB' global database of crust, mantle and core phase picks (1964-2007).
- 87,184 absolute P-wave delay times from temporary networks in Africa from 1994-2019 calculated using AARM (Boyce et al., 2017).
- Rays corrected for crust (next slide) elevation and ellipticity; traced through ak135 1D model and clustered.
- Global adaptive grid of spherical constant-velocity blocks controlled by ray density.
- Linear regularised inversion solved using LSQR (Li et al., 2008).
- Solve for slowness and hypocentre mislocation to minimise: $\varepsilon = ||wGm - wd||^2 + \lambda_1 ||Lm||^2 + \lambda_2 ||m||^2$
- G = sensitivity matrix, L = smoothing operator, w = data set weights.

1.

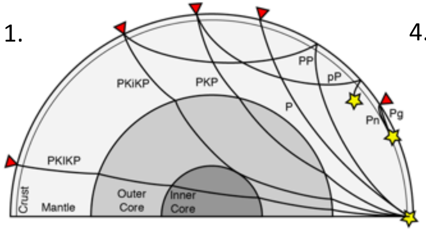

2.

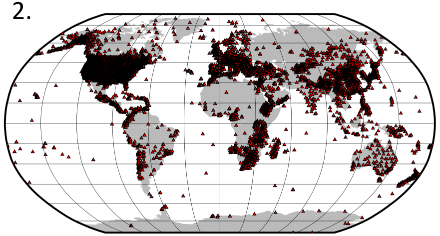

3.

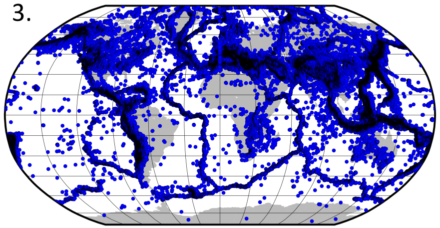

4.

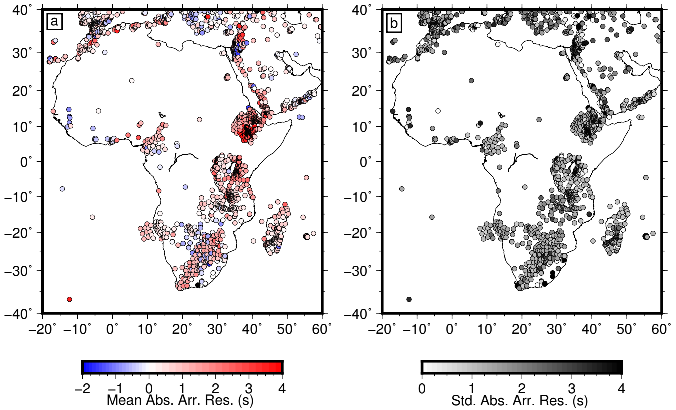

1. Schematic of P-phases used in `EHB' and AARM-derived database.
2. Global Seismograph station map.
3. Global Earthquake location map.
4. Mean (a) and standard deviation (b) of the direct-P phase absolute arrival-time residuals for the `EHB' database (Engdahl et al., 1998; Li et al. 2008) and augmented AARM-derived African data.

AFRP20 includes a Modified CRUST1.0

- We compile receiver function (RF) Moho depth estimates across Africa (a) from Akpan et al. (2016); Hosny and Nyblade (2016); Andriampenomanana et al. (2017); Ebinger et al. (2017); Lemnifi et al. (2017); Fadel et al. (2018); Ogden et al. (2019) and use these to improve the Moho depth within Crust1.0 (b - Laske et al., 2013).
- RF Moho depths interpolated and blended into CRUST1.0 (c).
- Use bespoke Moho depth model to scale depths to layer interfaces in upper 120km of ak135.
- Estimated contribution of bespoke crustal model is removed from each residual prior to inversion.

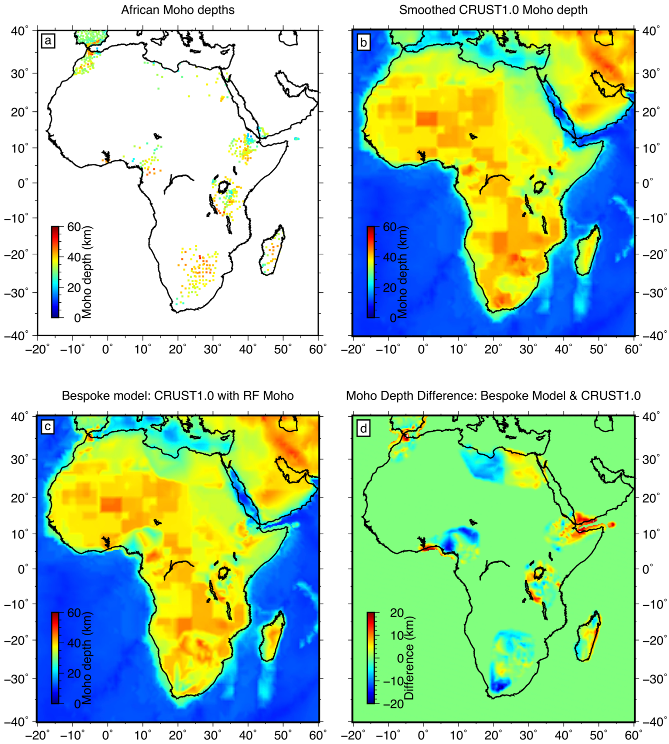

AFRP20 reveals slow wavespeeds below Cenozoic Magmatism

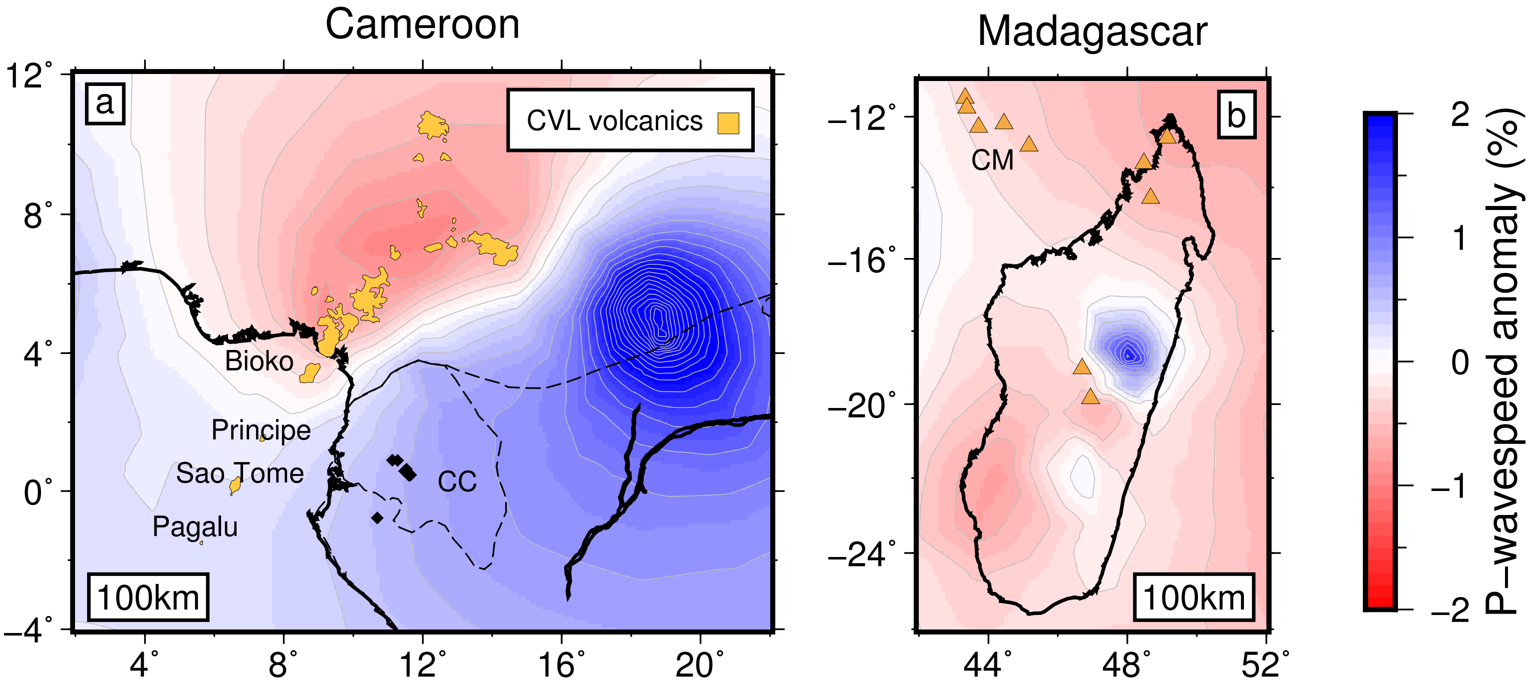

AFRP20 resolution tests

- Structural and checkerboard tests appraise the resolving power of AFRP20.
- Calculate arrival-time residuals through synthetic wavespeed models using identical ray paths to the observed data.
- Inversion performed following addition of 0.2s standard deviation Gaussian noise.
- Visual defects arise from imposing our input wavespeed models onto the coarse adaptive grid in poorly sampled regions.
- `Two Plume' resolution tests based on synthetic model rendered in 3D (a).

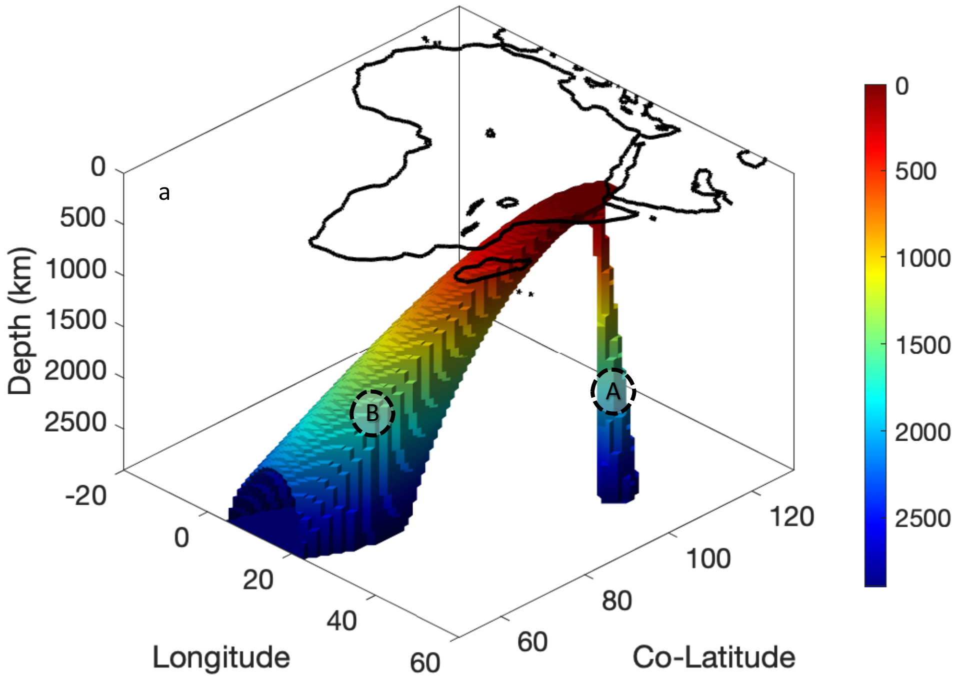

AFRP20 resolution tests: East African Mantle Plumes

1.

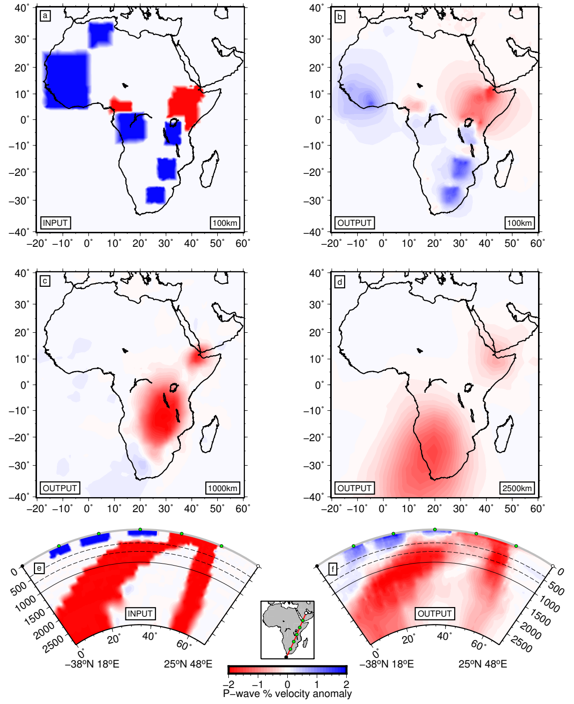

2.

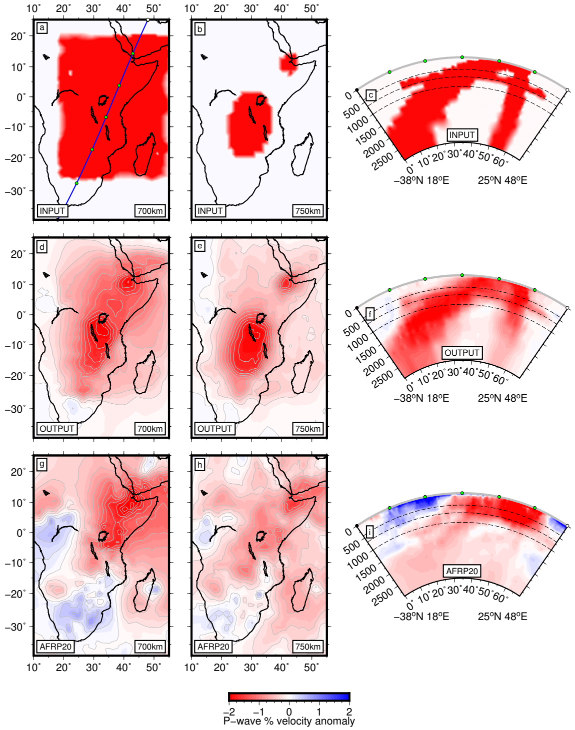

TAKE-HOME:

Two plumes converging on the upper mantle below East African rift is resolvable, with some amplitude loss in lower mantle.

Little evidence for ponded slow wavespeeds at/below mantle transition zone depths.

AFRP20 resolution tests: East African Mantle Plumes

1.

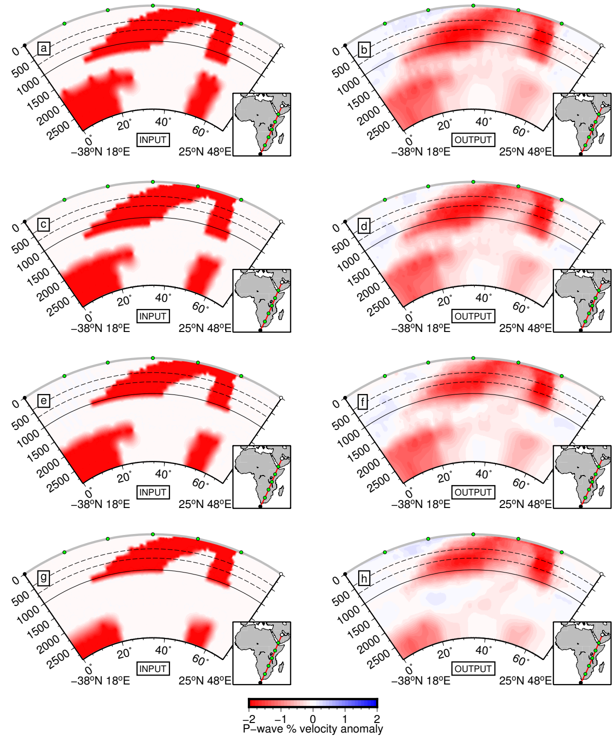

2.

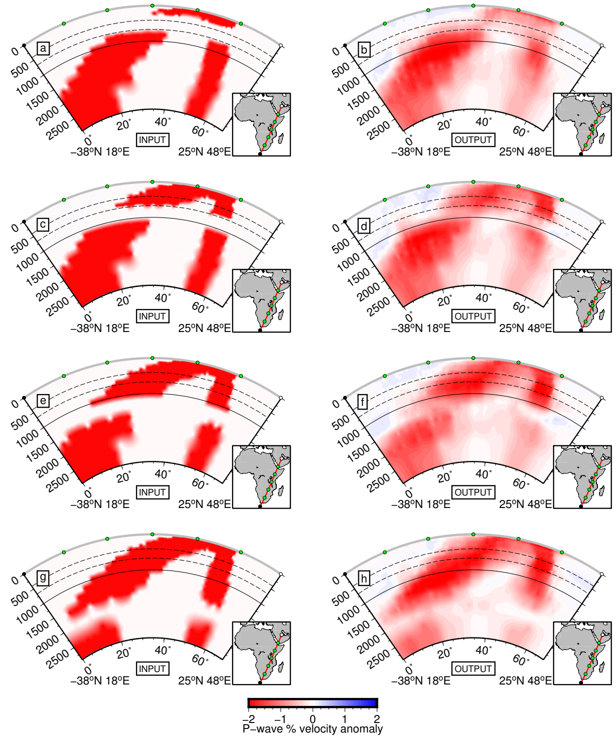

TAKE-HOME:

We expect to resolve a >300km discontinuity in slow wavespeed structure where amplitudes reduce to <40% of over-or-underlying anomaly.

AFRP20 resolution tests: Madagascar and Cameroon Volcanic Line

1.

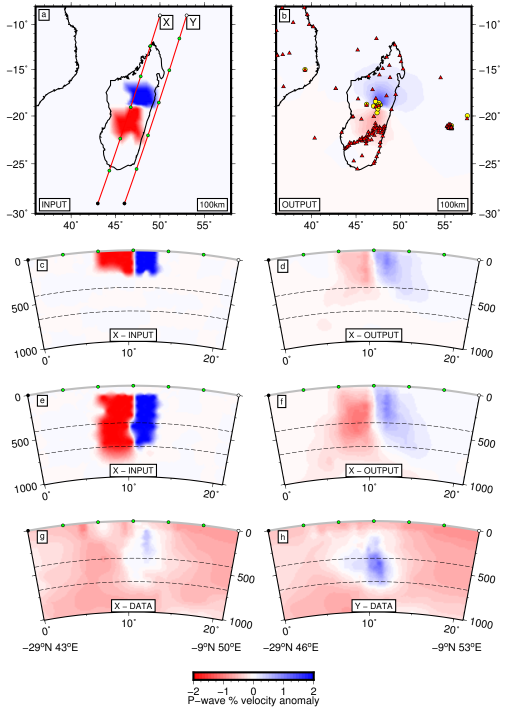

2.

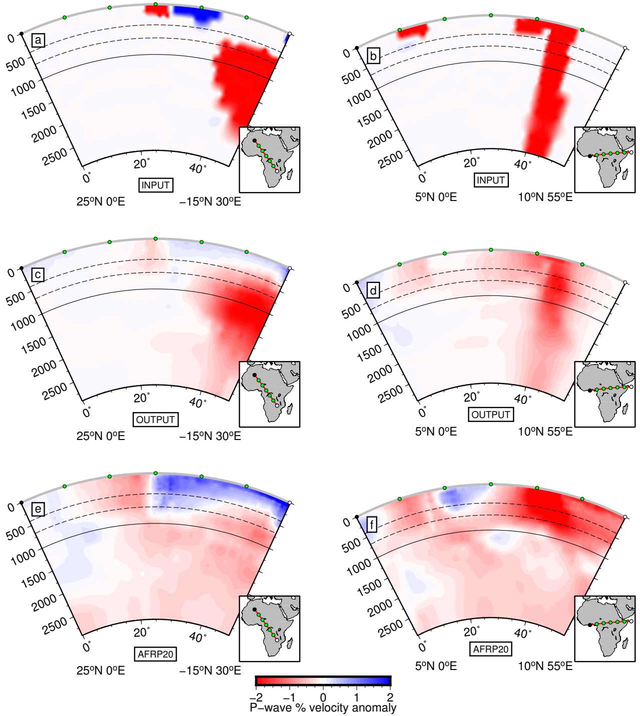

TAKE-HOME:

Vertical smearing, although significant, does not account for all of the slow wavespeed structure extending below the upper mantle in Madagascar (1) and Cameroon (2).

AFRP20 resolution tests: Turkana Depression

1.

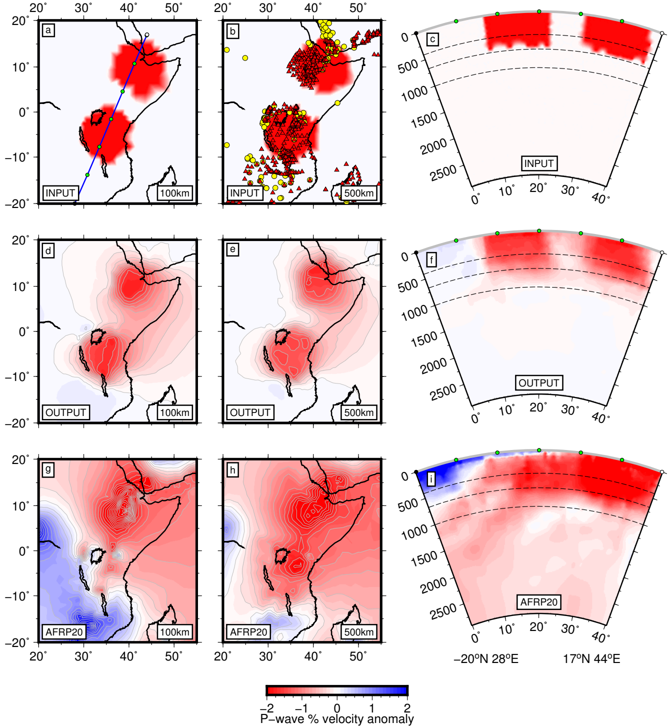

2.

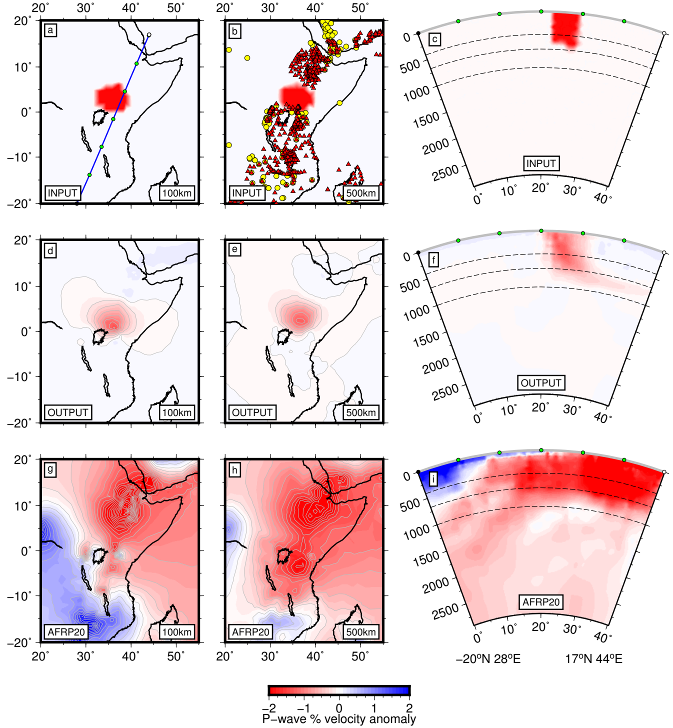

TAKE-HOME:

Ambient upper mantle below Turkana would yield muted wavespeeds (1d-f).

Slow upper mantle wavespeeds below Turkana are reasonably well resolved (2d-f).

AFRP20 resolution tests: Tanzanian craton

1.

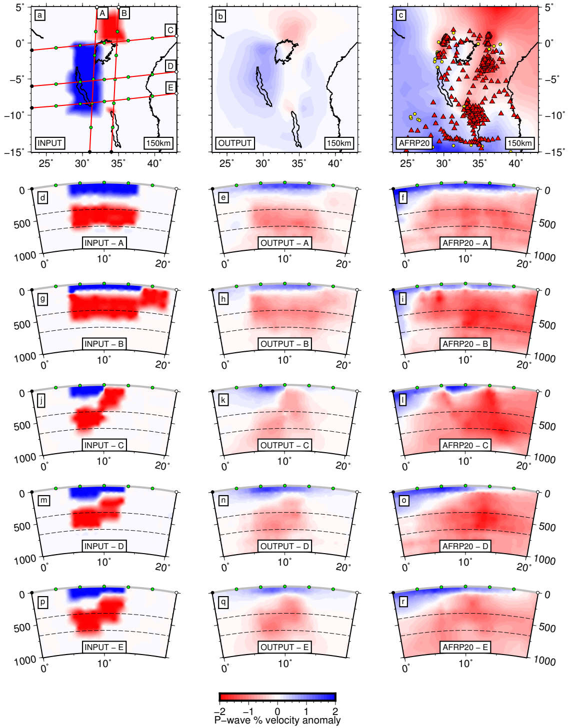

2.

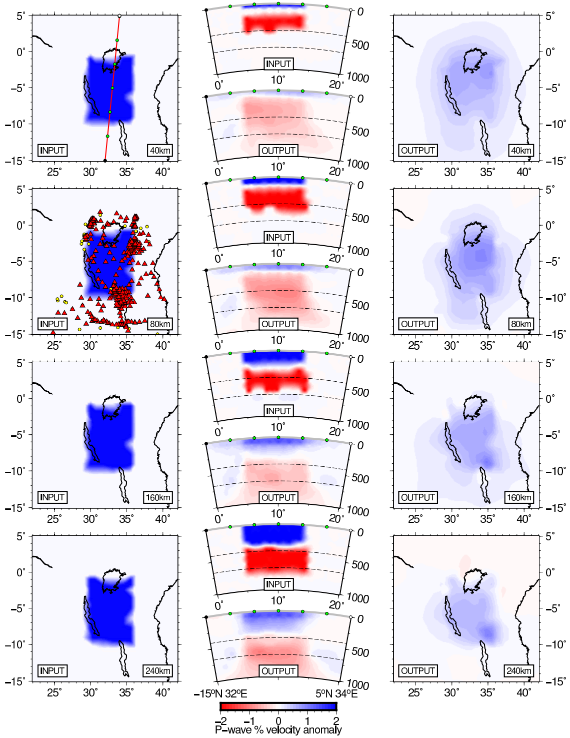

TAKE-HOME:

Asymmetrical fast wavespeeds below the Tanzanian craton can be resolved due to overlying station density, >1000Pn phases in EHB database recorded in region and presence of underlying slow wavespeeds.

AFRP20 resolution tests: Checkerboard Tests

1.

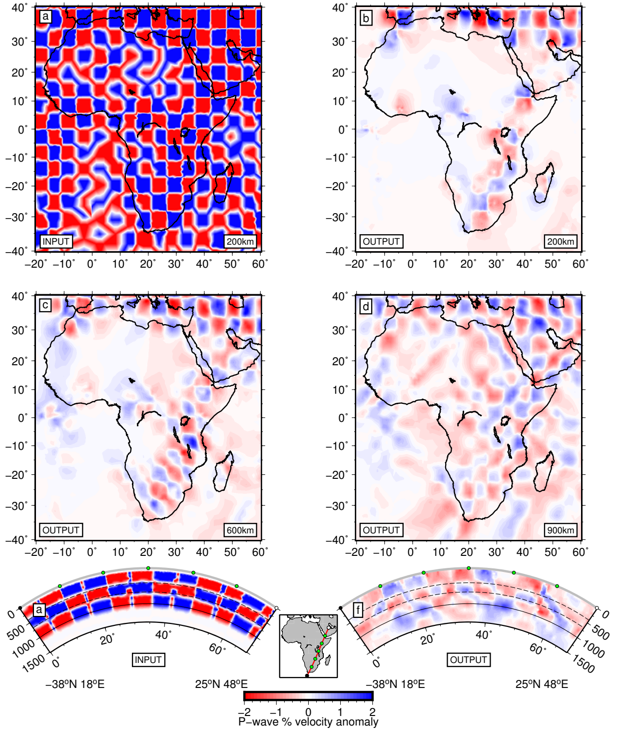

2.

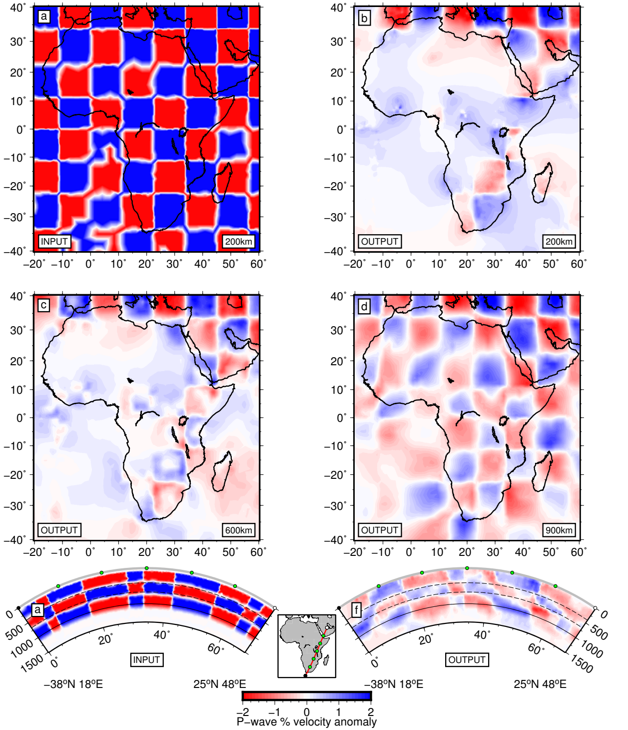

TAKE-HOME:

Sharp lateral boundaries of 5-10° anomalies are well recovered below good station coverage.

5-10° anomalies have reasonable resolvability in depth.

3D render: AFRP20 dVp=-0.5%

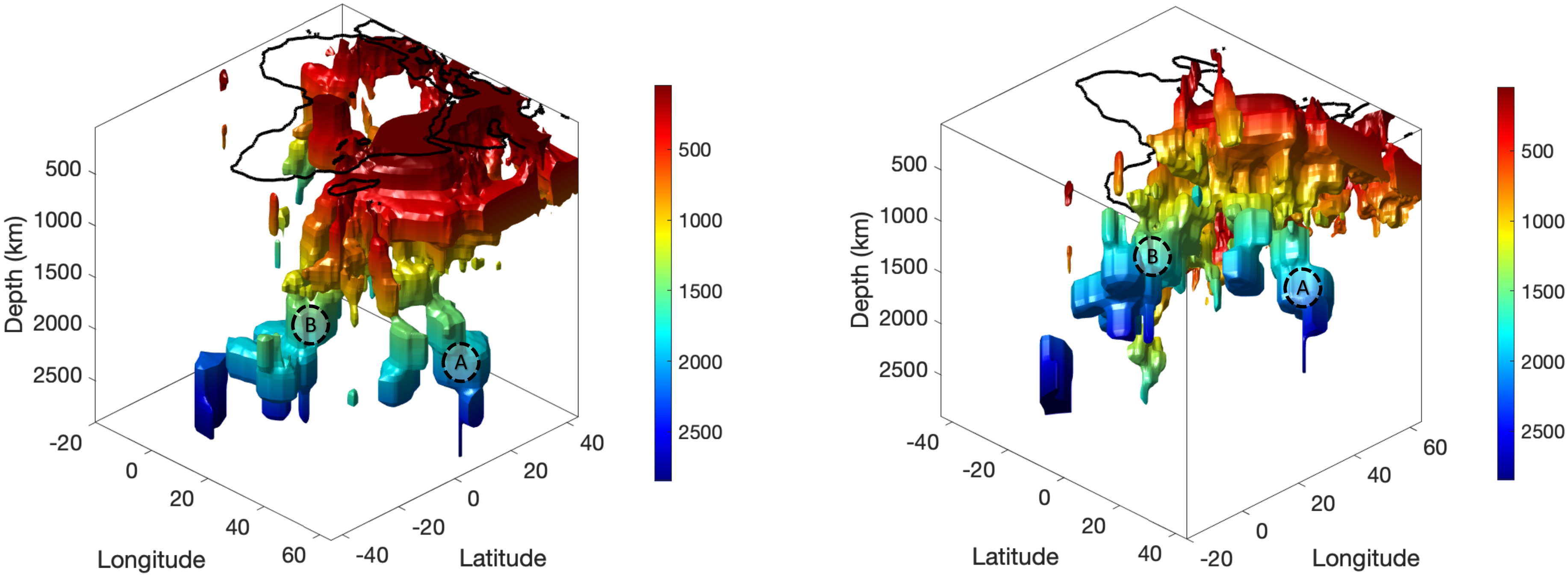

3D render: AFRP20 dVp=-0.5%

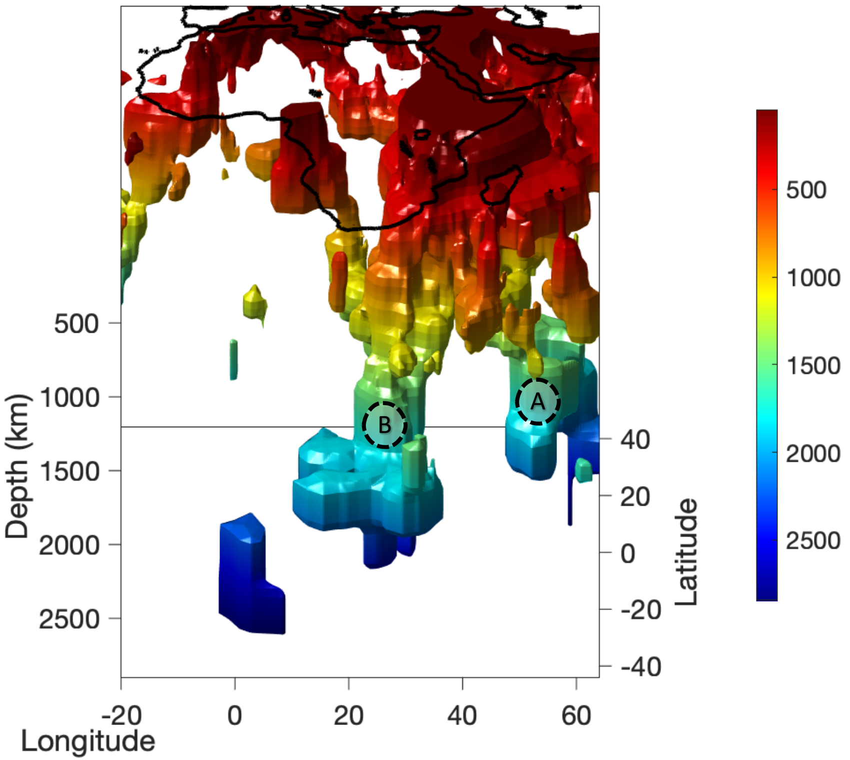

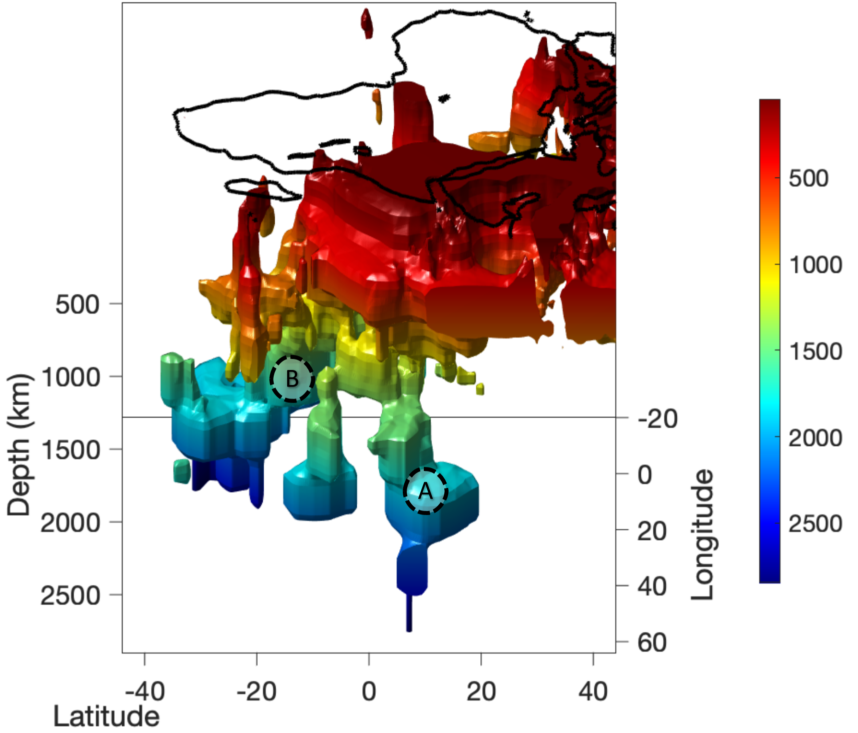

Comparisons of AFRP20 to other P-wave tomographic models

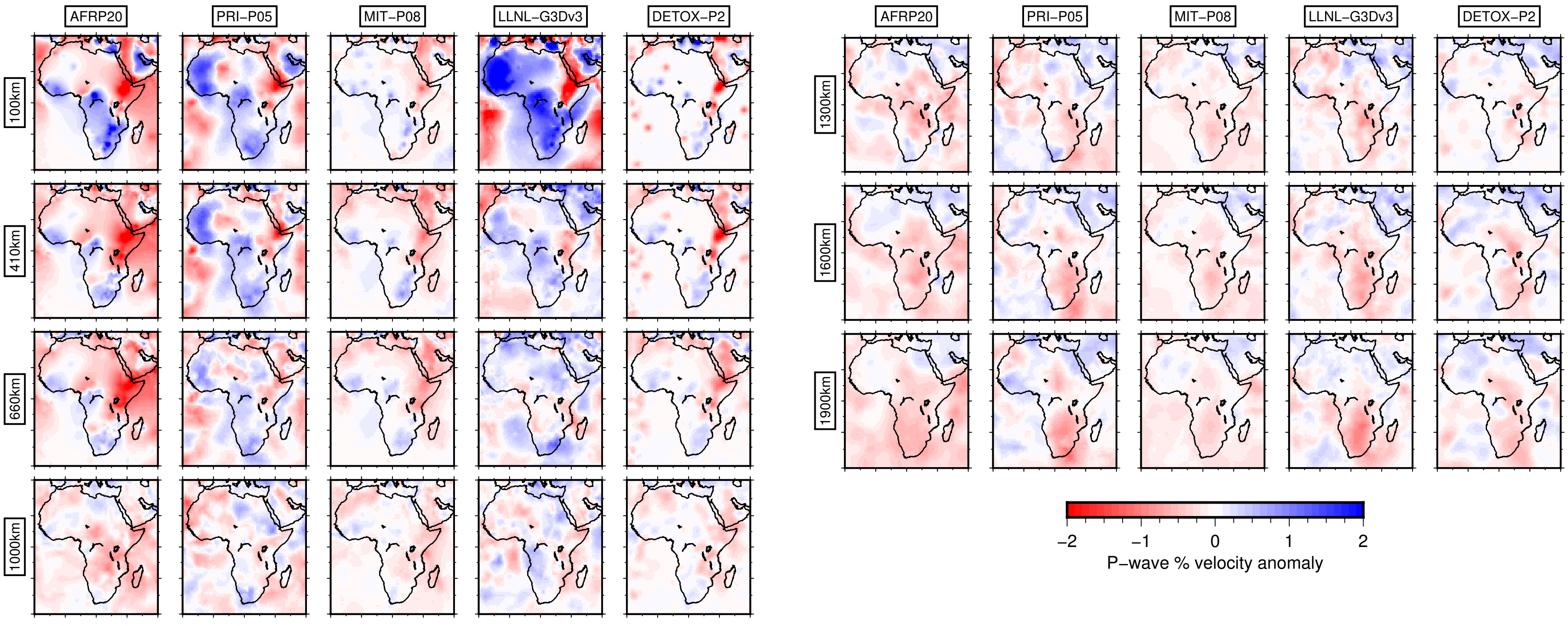

PRI-P05 (Montelli et al., 2006); MIT-P08 (Li et al., 2008); LLNL-G3Dv3 (Simmons et al., 2012); DETOX-P2 (Hosseini et al., 2019)

African Mantle Transition Zone Receiver Functions

Receiver Function Quality Control

Automated QC adapted from Cottaar and Deuss (2016).

We exclude RFs when:

- Direct P-arrival (max amplitude) does not occur within 2s of zero.
- RF reconvolved with the Z component reproduces less than 60 % of the R component.
- RF pre- and post peak amplitudes are greater than 40 % and 70 % of direct-P
- Signal-to-noise ratio of vertical (SNR < 2.5) and radial (SNR < 1.75).

We define SNR as:

$SNR = A_{post-arrival} / A_{pre-arrival}$

where A is RMS amplitude for 60s window separated by a 5s around the predicted arrival time for the direct-P.

RF Epicentral Distance Stacks

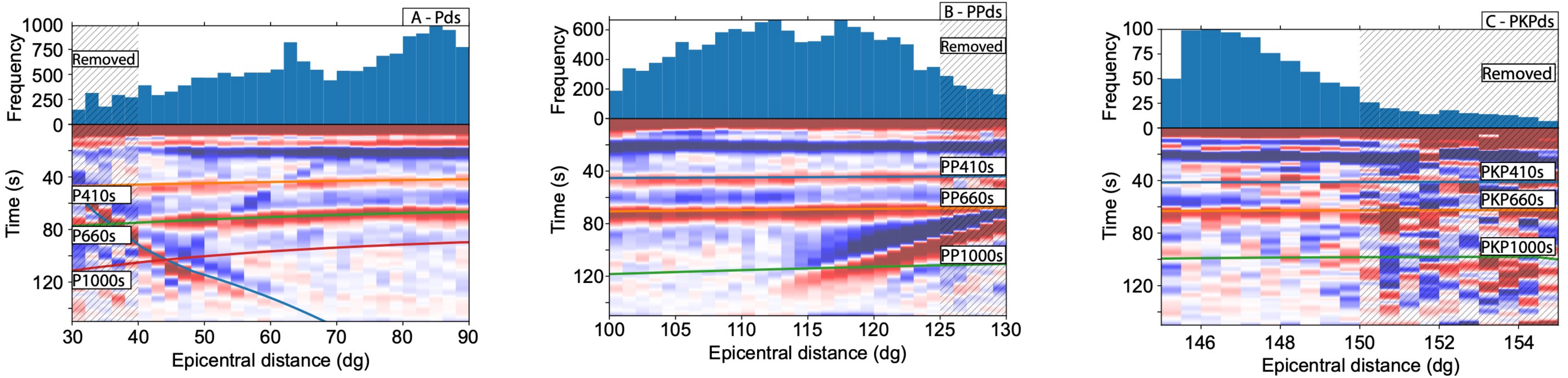

- RF stacks (data pre-filtered at 0.01-0.2Hz) binned by epicentral distance (Pds – A, PPds - B, PKPds – C).
- `Removed' distances are excluded from subsequent CCP stacking due to interfering phases.

RF Depth and Slowness stacks

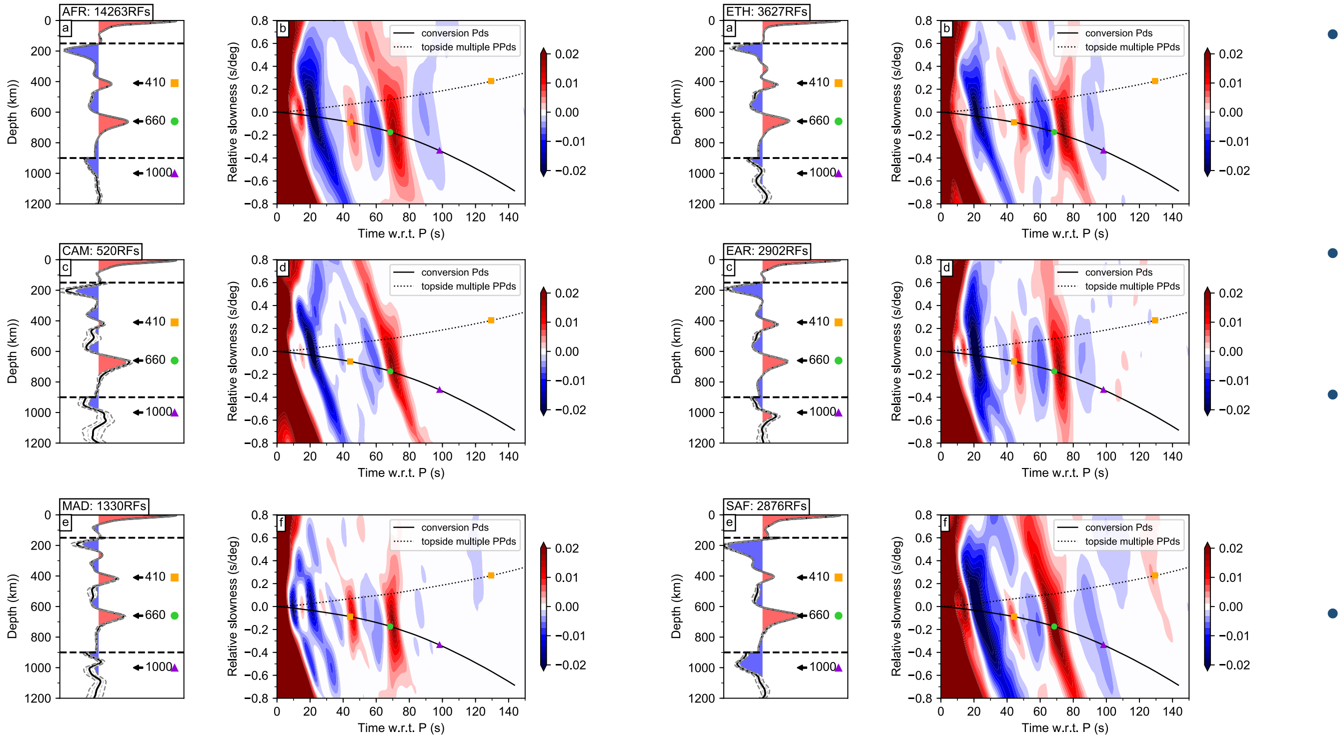

- Depth and slowness stacks for RFs for which pierce points at 410km depth fall within the given region.
- Depth stacks comprise RFs corrected to depth using AFRP20.
- Outwith the d410 below CAM, all regions show clear conversions from the d410 and d660 at the expected slowness.
- Only EAR shows a clear arrival from ~1000 km at the expected slowness.

UNIVERSITY OF CAMBRIDGE

NERC SCIENCE OF THE ENVIRONMENT

CCP stacking weights

- Grid of points spaced 0.5° in latitude and longitude and 2 km in depth within (0°E–52°E, –36°N–27°N, 0–1300 km depth).
- RF energy is back-propagated along raypaths and is stacked into proximal grid points at distances within two-times the fresnel-zone half width (Δ^{HW}) from the raypath by a weighing function (Lekic et al., 2011)

$$\Delta^{HW} = \sqrt{(\frac{\lambda}{3} + z)^2 - z^2}$$

- λ is the wavelength of a 10s shear wave and z is depth.
- Summed stacking weights and the standard error are tracked throughout the grid volume.
- We can expect to constrain discontinuity depths in regions where the summed weight is above 2 and amplitudes are greater than twice the standard error from the mean.

Common Conversion Point stacking: Weights

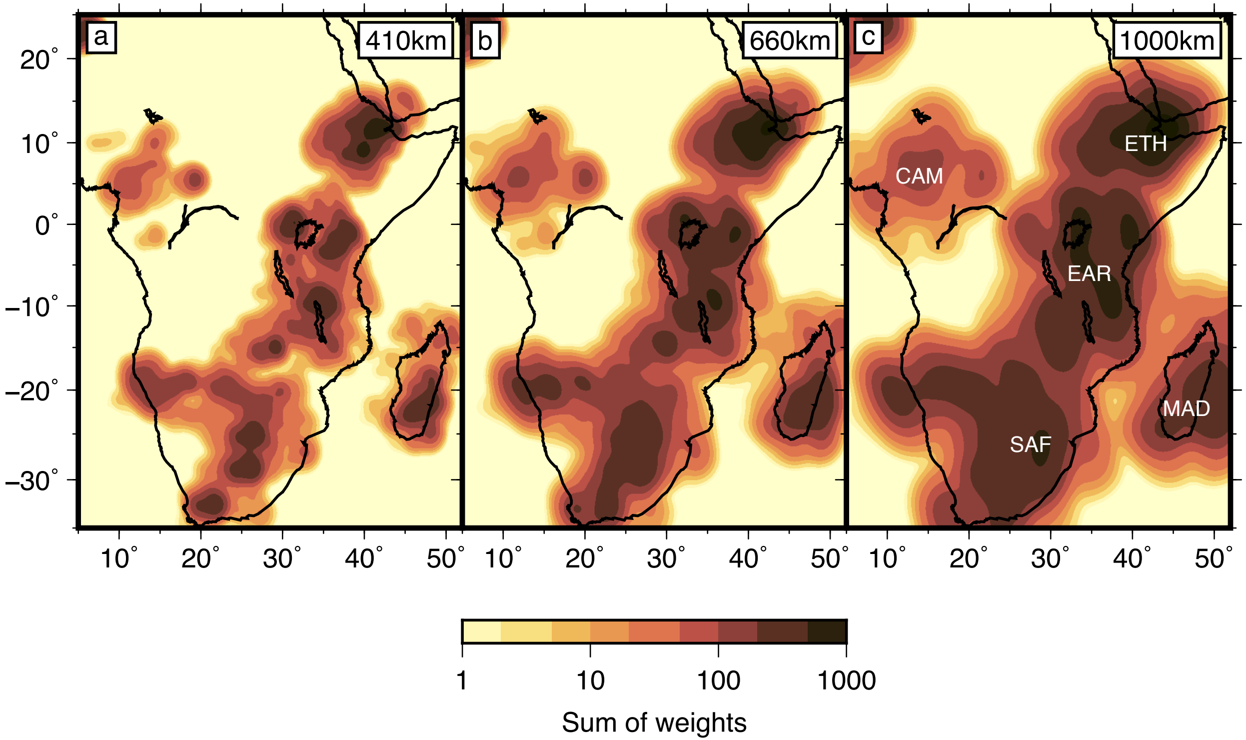

- CCP stacking weights are controlled by overlying station coverage.

Common Conversion Point stacking: ak135-CCP

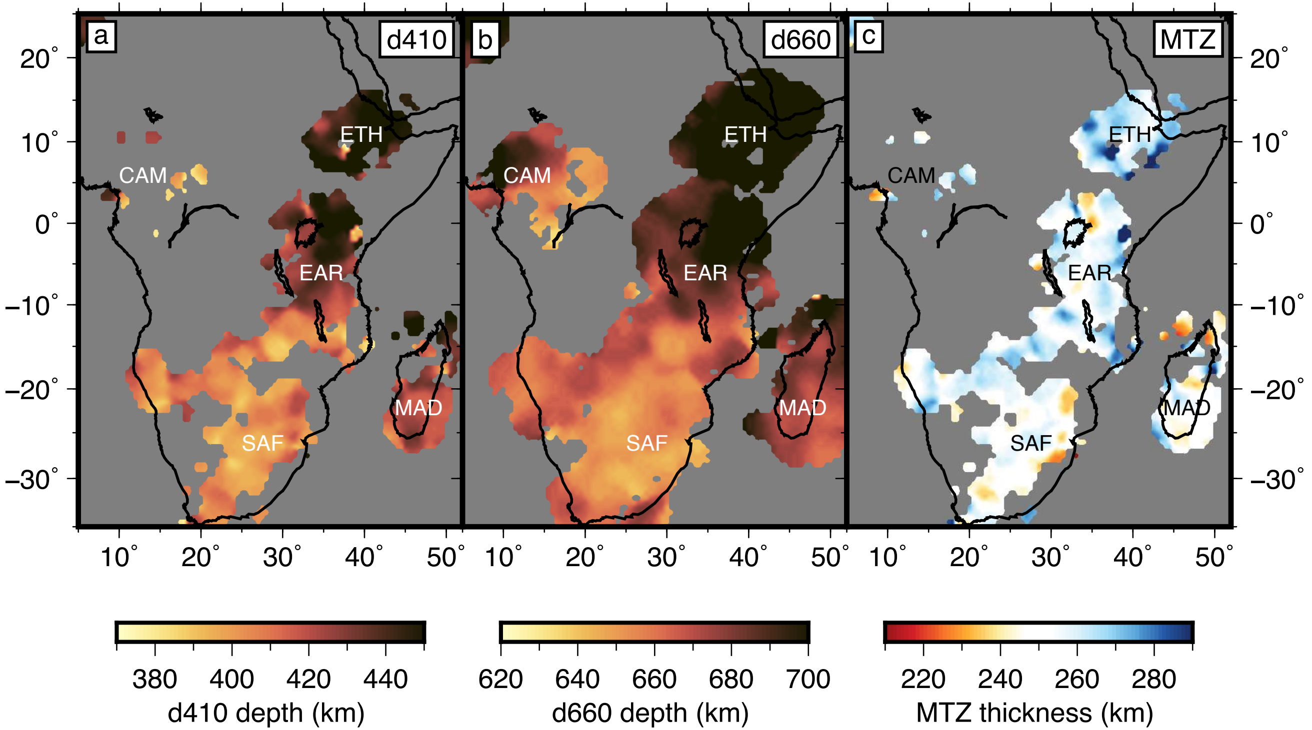

- Topography on the d410 and d660 shows strong correlation, with overall uplift beneath SAF and depression beneath EAR and ETH.
- Positive d410-d660 correlation typically indicates inadequate account for upper mantle wavespeed structure (e.g., Van Stiphout et al., 2019).

Quantitative assessment of time-to-depth correction

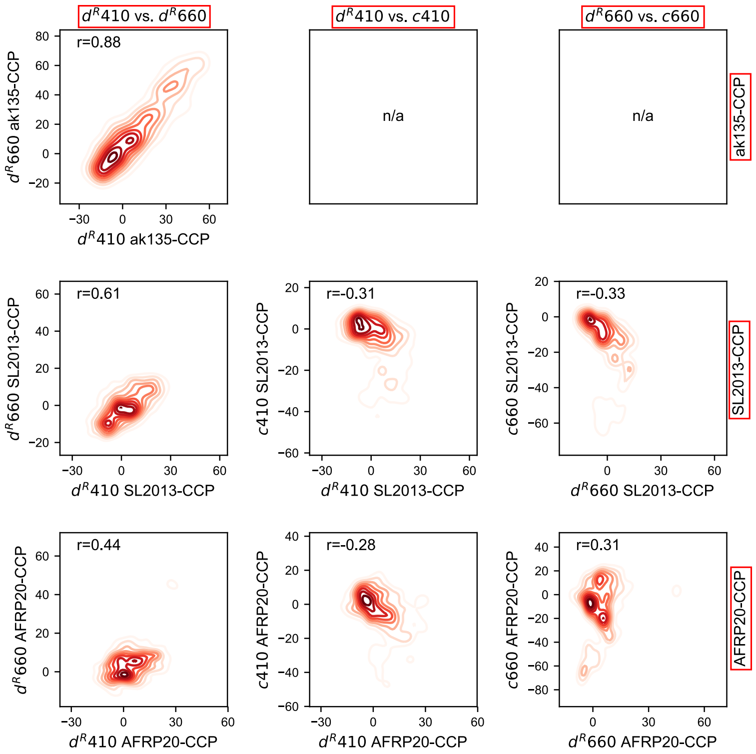

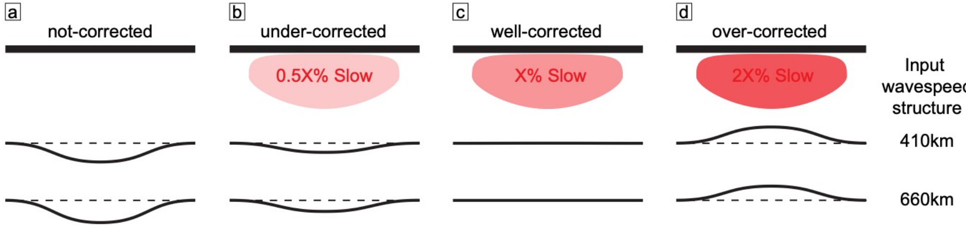

- Following Van Stiphout et al., (2019) we can quantitatively assess the time-to-depth correction of MTZ RFs using correlation between relative d410 and d660 depths (d^R410, d^R660) and topographic corrections compared to 1D velocity model (c410, c660).
- Require:
  - LOW: **r**[d^R410 : d^R660]
  - NEGATIVE: **r**[d^R410 : c410]
  - POSITIVE: **r**[d^R660 : c660]

Best performance:
AFRP20-CCP

Frequency dependence of MTZ depths

1.

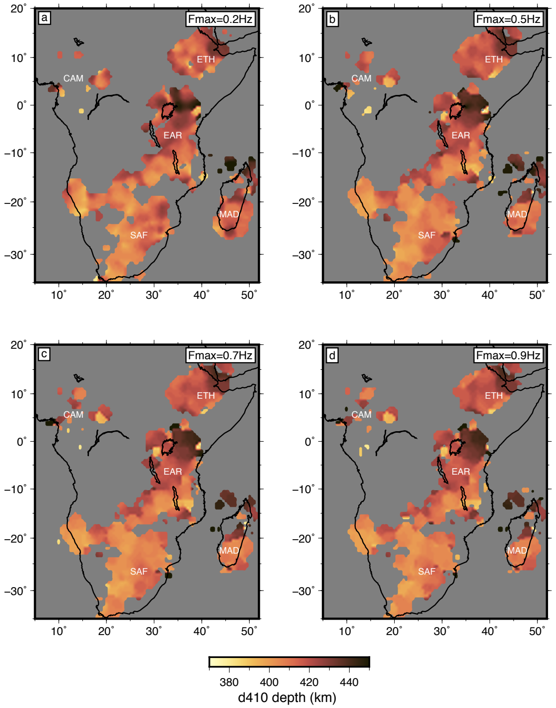

2.

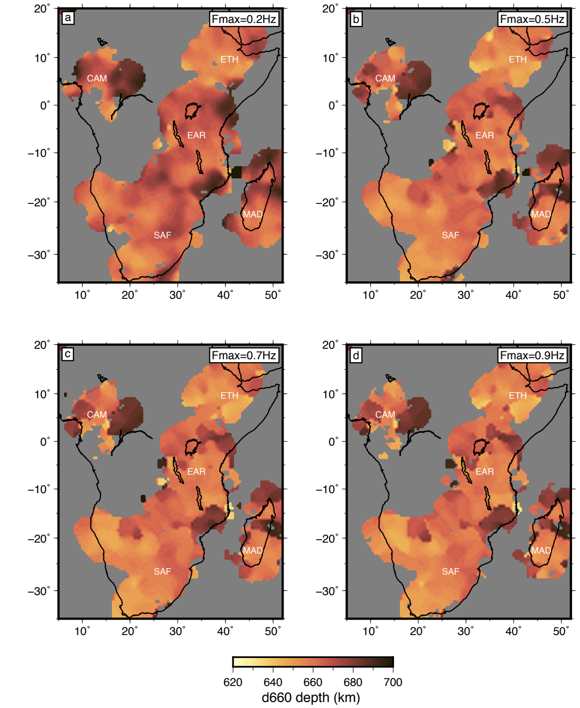

TAKE-HOME:

Maps of d410 (1) d660 (2) depth for AFRP20-CCP computed using RFs with maximum frequencies ranging from 0.2–0.9Hz.

d410 (1) depth does not change as a function of frequency, whilst the d660 (2) varies beneath EAR.

MTZ temperature estimates from mineral physics constraints

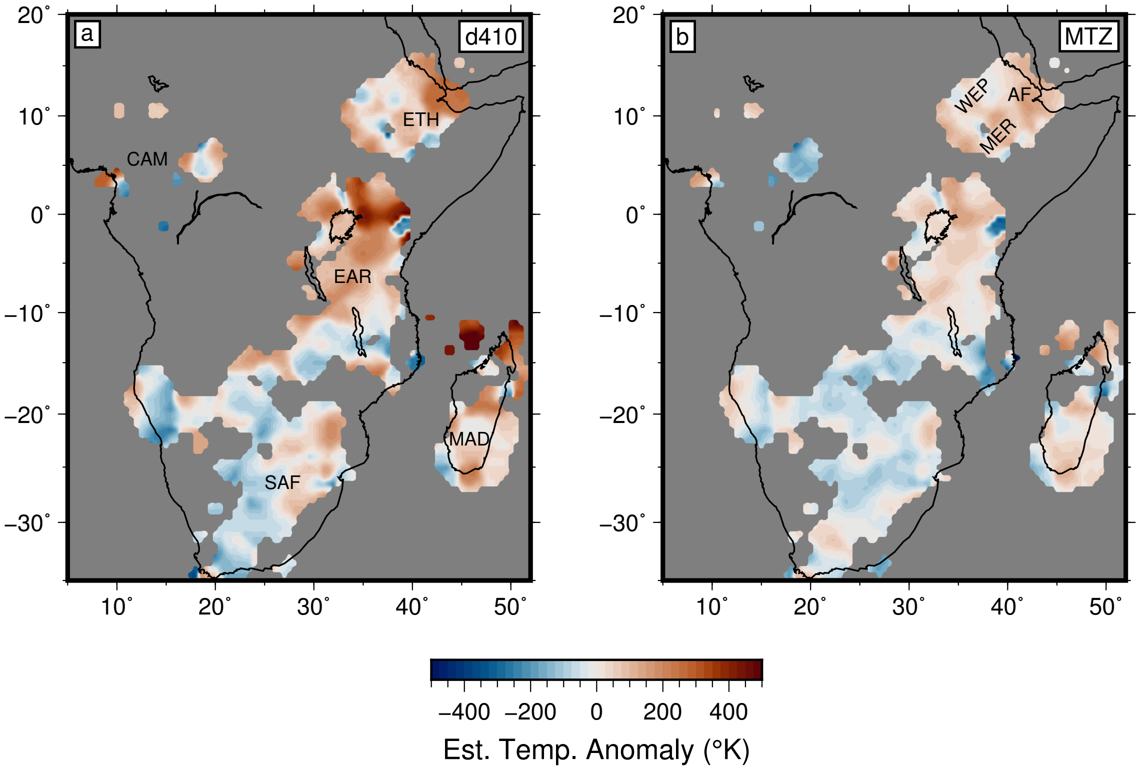

- a) temperature anomaly derived from d410 depths. We assume the temperature anomaly where d410 depth equals 410 km is zero. We assume an average value for the d410 Clapeyron slope of δP/δTd410=3.0 MPa/K (Bina & Helffrich, 1994).
- b) temperature anomaly derived from MTZ thickness. We assume the temperature anomaly is zero where MTZ thickness is 250 km. We use the same Clapeyron slope for the d410 as in a and an average d660 Clapeyron slope of δP/δTd660=–2.5 MPa/K (Ye et al., 2014) for the olivine transition.
- Similarity between d410 depth and MTZ thickness derived temperature anomaly estimates indicates regional d410 depths are reliable and the d660 is not controlled by the garnet transition, i.e. a pyrolitic composition dominates.
- ETH peak MTZ thermal anomalies: 100-150°K.
- EAR peak MTZ thermal anomalies: 225-450°K.

Discontinuities at 1000km depth indicate a compositional anomaly

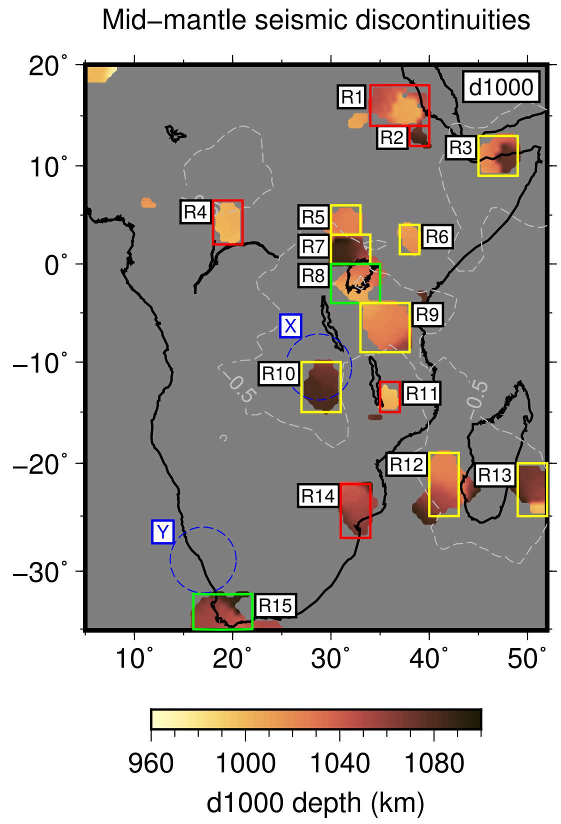

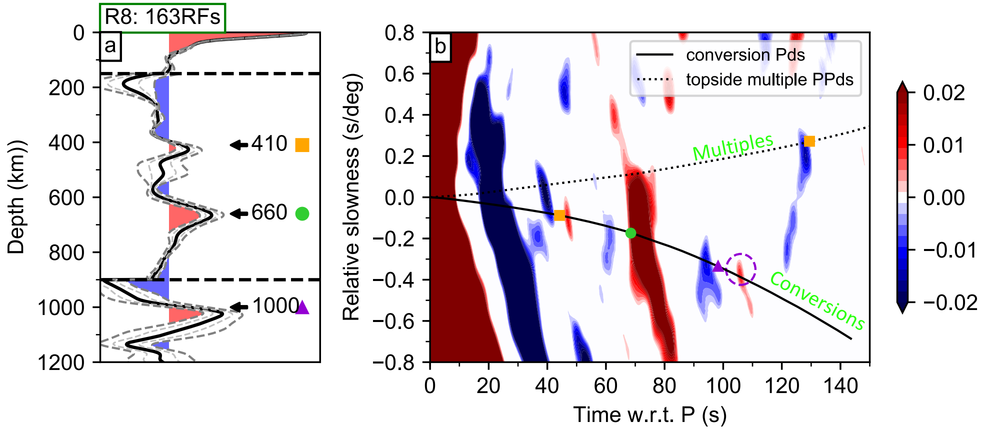

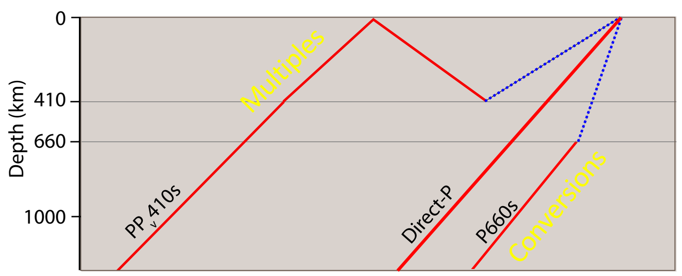

- Slowness stacks are used to decipher between conversions and multiples.
- Slowness stacks of R8 and R15 reveal robust mid-mantle conversions.

Resources:

Tomography:

- AARM available at: https://github.com/alistairboyce11/AARM
- Distribution of AFRP20 tomographic model to be made available upon publication at IRIS EMC: http://ds.iris.edu/ds/products/emc-earthmodels/
- Matlab script to render tomography in 3D: https://github.com/alistairboyce11/3D_Tomo_Iso
- Manuscript: **Boyce, A**. Bastow, I.D. Cottaar, S. Kounoudis, R. Guilloud De Courbeville, J. Caunt, E. Desai, S. (*submitted*) AFRP20: New P-wavespeed Model for the African Mantle Reveals Two Whole-Mantle Plumes Below East Africa and Neoproterozoic Modification of the Tanzania Craton (*in revision: G-cubed).*

Receiver Functions:

- Toolkit for Utilizing Receiver Functions in Python (TURFPY) available at: https://github.com/sannecottaar/turfpy
- Text file of MTZ discontinuity depths below Africa to be made available with publication.
- Manuscript: **Boyce, A**. Cottaar, S. (*submitted)* Insights into Deep Mantle Thermochemical Contributions to African Magmatism from Converted Seismic Phases (*under review at G-cubed).*

References

Akpan, O., et al., (2016). Crustal structure of Nigeria and Southern Ghana, West Africa from P-wave receiver functions. Tectonophysics, 676, 250–260.
Andriampenomanana, F., et al., (2017). The structure of the crust and uppermost mantle beneath Madagascar. Geophys. J. Int., 210(3), 1525–1544.
Bina, C. R., & Helffrich, G. R. (1994). Phase transition Clapeyron slopes and tran- sition zone seismic discontinuity topography. J. Geophys. Res., 99(B8), 15853.
Boyce, A., et al., (2017), From relative to absolute teleseismic travel-times: the Absolute Arrival-time Recovery Method (AARM), Bull. Seis. Soc. Am., **107(5)**, 2511–2520.
Chang, S. J., & Van der Lee, S. (2011). Mantle plumes and associated flow beneath Arabia and East Africa. Earth Planet. Sci. Lett., 302(3-4), 448–454.
Civiero, C., et al., (2015). Multiple mantle upwellings in the transition zone beneath the northern East-African Rift system from relative P-wave travel- time tomography. Geochem. Geophys. Geosyst., 16(9), 2949–2968.
Cottaar, S. & Deuss, A., (2016). Large-scale mantle discontinuity topography beneath Europe: Signature of akimotoite in subducting slabs. J. Geophys. Res., **121(1)**, pp.279-292.
Cottaar, S., & Lekic, V. (2016). Morphology of seismically slow lower-mantle struc- tures. Geophys. J. Int., 207(2), 1122–1136.
Dziewonski, A. M., & Anderson, D. L. (1981). Preliminary reference Earth model. Phys. Earth Planet. Int., 25(4), 297–356.
Ebinger, C. J., & Sleep, N. (1998). Cenozoic magmatism throughout East Africa resulting from impact of a single plume. Nature, 395, 788-791.
Ebinger, C. J., et al., (2017). Crustal Structure of Active Deformation Zones in Africa: Implications for Global Crustal Processes. Tectonics, 36(12), 3298– 3332.
Fadel, I., et al., (2018). Crustal Structure and Dynamics of Botswana. J. Geophys. Res., 123(12), 10,659–10,671.
George, R., et al., (1998). Earliest magmatism in Ethiopia: evidence for two mantle plumes in one continental flood basalt province. Geology, 26, 923-926.
Halldórsson, S. A., et al., (2014). A common mantle plume source beneath the entire East African Rift System revealed by coupled helium-neon systematics. Geophys. Res. Lett., 41(7), 2304–2311.
Hansen, S. E., et al., (2012). Mantle structure beneath Africa and Arabia from adaptively parameterized P-wave tomography: Implications for the origin of Cenozoic Afro-Arabian tectonism. Earth Planet. Sci. Lett., 319, 23–34.
Hilton, D. R., et al., (2011). Helium isotopes at Rungwe Volcanic Province, Tanzania, and the origin of East African Plateaux. Geophys. Res. Lett., 38(21).
Hosny, A., & Nyblade, A. A. (2016). The crustal structure of Egypt and the northern Red Sea region. Tectonophysics, 687, 257–267.
Hosseini, K., et al., (2019). Global mantle structure from multifrequency tomography using P, PP and P-diffracted waves. Geophys. J. Int., 220(1), 96–141.
Jenkins, J., et al., (2016), Depressed mantle discontinuities beneath Iceland: Evidence of a garnet controlled 660 km discontinuity?. Earth Planet. Sci. Lett., **433**, pp.159-168.
Kennett, B.L.N., et al., (1995), Constraints on seismic velocities in the earth from traveltimes. Geophys. J. Int., **122**, 108–124.
Laske, G., et al., (2013, April). Update on CRUST1.0 - A 1-degree Global Model of Earth’s Crust. In Geophys. res. abstracts, 15, abstract egu2013-2658 (p. EGU2013-2658).
Lekic, V., et al., (2011). Lithospheric Thinning Beneath Rifted Regions of Southern California. Science, 334(6057), 783–787.
Lemnifi, A. A., et al., (2017). Crustal Thickness Beneath Libya and the Origin of Partial Melt Beneath AS Sawda Volcanic Province From Receiver Function Constraints. J. Geophys. Res., 122(12), 10,037–10,051.
LeStunff, Y., et al., (1995). P’P’ Precursors Under Africa: Evidence for Mid-Mantle Reflectors. Science, 270(5233), 74–77.
Li, C., et al., (2008), A new global model for P wave speed variations in Earth’s mantle, Geochem.Geophys. Geosyst., **9**, Q05018.
Ligorria, J.P. & Ammon, C.J., (1999), Iterative deconvolution and receiver-function estimation. Bull. Seis. Soc. Am., **89(5)**, pp.1395-1400.
Montelli, R., et al., (2006). A catalogue of deep mantle plumes: new results from finite-frequency tomography. Geochem. Geophys. Geosyst., 7, Q11007.
Ogden, C. S., et al., (2019). A reappraisal of the H–κ stacking technique: implications for global crustal structure. Geophys. J. Int., 219(3), 1491–1513.
Pik, R. (2011). Geodynamics: East Africa on the rise. Nat. Geosci., 4(10), 660–661.
Rogers, N. W., et al., (2000). Two mantle plumes beneath the East African rift system: Sr, Nd and Pb isotope evidence from Kenya Rift basalts. Earth Planet. Sci. Lett., 176, 387-400.
Rogers, N. W., et al., (2010). Osmium iso- topes and Fe/Mn ratios in Ti-rich picritic basalts from the Ethiopian flood basalt province: No evidence for core contribution to the Afar plume. Earth Planet. Sci. Lett., 296(3-4), 413–422.
Schaeffer, A.J. & Lebedev, S. (2013), Global shear speed structure of the upper mantle and transition zone, Geophys. J. Int., **194(1)**, 417–449.
Simmons, N. A., et al., (2012). LLNL-G3Dv3: Global P wave tomography model for improved regional and teleseismic travel time prediction. J. Geophys. Res., 117(B10). doi: 10.1029/2012jb009525
VanDecar, J., & Crosson, R. (1990). Determination of teleseismic relative phase arrival times using multi-channel cross-correlation and least squares. Bull. Seis. Soc. Am., 80(1), 150-169.
Van Stiphout, et al., (2019). Receiver function mapping of mantle transition zone discontinuities beneath Alaska using scaled 3-D velocity corrections Geophys. J. Int., 219(2), 1432-1446.
Ye, Y., et al., (2014). The postspinel boundary in pyrolitic compositions determined in the laser-heated diamond anvil cell. Geophys. Res. Lett., 41(11), 3833–3841.